

## Article

# Genesis and Geological Significance of Siderite in the First Member of the Nantun Formation of Dongming Sag, Hailar Basin

Mingxian Xie <sup>1,2</sup>, Feng Ma <sup>2,\*</sup>, Guangpo Chen <sup>2</sup>, Xi Zheng <sup>1,2</sup>, Rong Xiao <sup>3</sup> and Chengjun Zhang <sup>1</sup>

<sup>1</sup> School of Earth Sciences, Key Laboratory of Mineral Resources in Western China (Gansu Province), Lanzhou University, Lanzhou 730000, China

<sup>2</sup> Research Institute of Petroleum Exploration & Development–Northwest, PetroChina, Lanzhou 730020, China

<sup>3</sup> Yanchang Oil Field Co., Ltd., Yan'an 718600, China

\* Correspondence: mafeng@petrochina.com.cn

**Abstract:** Multiple siderite beds developed in the first member of the Lower Cretaceous Nantun Formation ( $K_1n^1$ ) in the basin. The results show that the siderites in  $K_1n^1$  of the study area are mostly stratiform or massive, with three micromorphological features (dense micronized crystals, bands, and paragenesis with quartz and calcite). The siderite beds are mainly composed of siderite, clay, quartz, calcite, and feldspar. Under the microscope, charcoal, algal fossils, granular pyrite crystals, vein-like siliceous bands, etc., were observed. The oxides in the siderite beds include  $Fe_2O_3$ ,  $SiO_2$ ,  $Al_2O_3$ , etc. The trace elements are typically characterized by high Mn and Be contents; low Sr/Ba, Th/U, and Al/Ti ratios; and high V/Cr ratios. These indicate weakly reducing, freshwater depositional paleoenvironments. The  $\delta^{13}C_{V-PDB}$  and  $\delta^{18}O_{V-PDB}$  values of siderite are  $-0.20$ – $1.11$ ‰ (mean:  $0.62$ ‰) and  $-18.22$ ‰ to  $-10.14$ ‰ (mean:  $-14.23$ ‰), respectively, which shows that the carbon in siderite came mainly from carbonate dissolution. The Fe-bearing rocks in the source area migrated to the basin after undergoing physical and chemical weathering, and when the resultant  $Fe^{2+}$  concentration reached saturation,  $Fe^{2+}$  combined with  $CO_3^{2-}$  in the water bodies to form authigenic siderite.

**Keywords:** Dongming sag; the first member of the Nantun Formation; siderite; major and trace elements; carbon and oxygen isotopes; paleoenvironment; genetic mechanism



**Citation:** Xie, M.; Ma, F.; Chen, G.; Zheng, X.; Xiao, R.; Zhang, C.

Genesis and Geological Significance of Siderite in the First Member of the Nantun Formation of Dongming Sag, Hailar Basin. *Minerals* **2023**, *13*, 804.

<https://doi.org/10.3390/min13060804>

Academic Editor: Dan Asael

Received: 9 April 2023

Revised: 5 June 2023

Accepted: 10 June 2023

Published: 13 June 2023



**Copyright:** © 2023 by the authors. Licensee MDPI, Basel, Switzerland. This article is an open access article distributed under the terms and conditions of the Creative Commons Attribution (CC BY) license (<https://creativecommons.org/licenses/by/4.0/>).

## 1. Introduction

Siderite is an important iron-bearing carbonate mineral often found in marine or lacustrine settings, with  $FeCO_3$  as its main component [1–4]. Siderite ( $FeCO_3$ , density  $3960\text{ kg/m}^3$ ; Hurlbut, 1971) is a brownish translucent mineral crystallizing in the same hexagonal (rhombohedral) lattice as calcite [5]. Large amounts will rarely be attained in an ore deposit because Fe carbonates tend to have a wide range of substitution of Mn, Mg, and Ca for bivalent Fe [6]. In recent years, scholars worldwide have carried out many studies on the characteristics, genetic mechanism, and formation environment of siderite. The genetic mechanism of siderite has long been the focus of debate [1,4–16]. Tu [17] believed that siderites are of either sedimentogenesis or hydrothermal genesis. Sedimentary siderites are commonly found in shale, clay, and coal beds, often in oolitic and nodular forms, and coexist with oolitic hematite, oolitic chlorite, and goethite. However, although hydrothermal siderites are often found in metalliferous veins, there can be a separate siderite vein or one associated with ankerite, galena, sphalerite, chalcopyrite, magnetite pyrite, and other deposits. Xie et al. [4] analyzed the petrography of different types of siderites and concluded that siderites of different forms correspond to three genetic processes: authigenesis, eodiagenesis (early diagenesis), and telodiagenesis (late diagenetic). They also concluded that siderites derived from different genetic processes have different significance to paleoenvironmental restoration. Frederichs et al. [5] believes that siderite

is an authigenic mineral in a number of sedimentary settings. It is restricted to anoxic non-sulfidic methanic environments, and occurs in rapidly accumulating, fine-grained, organic-rich sediments, where  $\text{CO}_2$  is produced as a result of oxidation of organic matter, partly by reduction of Mn and Fe oxyhydroxides. Köhler et al. [10] suggested that siderite was formed during dissimilatory iron reduction during the early diagenetic stage. Dill pointed out that siderite in clay rock and coal-bearing sandstone related to coal seams is usually produced as sphaerosiderite, a microcrystalline rhodochrosite. Moreover, near the edge of freshwater lakes, colloidal siderite is often produced in temperate climate [5]. Usually, its formation depends mainly on the Eh and pH conditions in the basin, which determine the variation of iron-bearing minerals from calcareous hematite, magnetite, and rhodonite to siliceous iron ore, and even pyrite. Siderite precipitates at an Eh below 0 (volt) and in the pH range 7 to 9, depending on the activities of the dissolved species Fe and C. Siderite disappears with decreasing activity of  $\text{HCO}_3^-$  at  $\log a\text{HCO}_3^- = -3$  and increasing activity of  $\text{HPO}_4^{2-}$  at  $\log a\text{HPO}_4^{2-} = -3$  [Burger et al.]. Zhang et al. [16] believed that the formation of siderites with different micromorphological features is closely related to sea-level fluctuation, which manifests as a cyclical change controlled by the sequence-stratigraphic framework. Additionally, Dill mentioned that a stratiform siderite ore deposit at Arzberg, Germany, intercalated with argillaceous metasediments is a product of post volcanic and microbiological processes [5]. Some scholars believe that siderite was transformed by organic matter reduction under reducing conditions [14–20]. Siehl and Thein [21] hold that siderite may be converted from silica-rich ferric oxides during diagenesis in a reducing environment. Burkhalter et al. [22] believed that microbial activity probably played also a key role during Fe accumulation in the near-shore environments. Other mechanisms, such as bacterial sulfate reduction, anaerobic oxidation of methane, and thermal decarboxylation of organic matter, can also provide carbon for the formation of siderite [23–25]. Despite the complex genesis of siderite, it is generally believed that authigenic siderite is typically formed when soluble, reducing  $\text{Fe}^{2+}$  is combined with  $\text{HCO}_3^-/\text{CO}_3^{2-}$  in an oxygen-deficient, iron-rich, low-sulfate environment. The formation of authigenic siderite is closely related to biological activities [3,26] and can directly indicate a high atmospheric  $\text{CO}_2$  concentration [4]. The formation of diagenetic siderite mainly reflects the active iron cycle process between water and sediments but cannot directly reflect the atmospheric  $\text{CO}_2$  concentration [4,18,19]. In continental petroliferous sedimentary basins, carbonate minerals such as calcite and dolomite have a greater impact on the hydrocarbon generation of source rocks [27–31].

Little research has been conducted to clarify whether siderite affects the hydrocarbon generation of source rocks. Nigam et al. [32] pointed out that the formation of siderite is very complex, and the diagenesis associated with siderite formation occurs at the same temperature as the transformation of organic matter to oil and gas. Milesi et al. [11] believed that the hydrogen derived from complete or partial oxidation or dissolution of highly mature kerogen in the heated source rocks reduces siderite to form methane and that the hydrocarbon gas generation from the decomposition of economically viable hydrothermal fluids with siderite may be widespread in petroliferous basins with high thermal stress. Zhang et al. [33,34] performed thermogravimetric experiments to study the effect of siderite on the pyrolysis of organic matter in source rocks of the Dameigou Formation in the northern margin of the Qaidam Basin and concluded that siderite can promote the pyrolysis of organic matter in source rocks. He mentioned that siderite would undergo thermal decomposition at high temperature of about 450–600 °C [33,34].

The present study meticulously analyzes the sedimentary environment and the petrological, geochemical, and isotopic characteristics of siderite developed in the source rocks of the first member of the Nantun Formation ( $K_1n^1$ ) in the Dongming sag, Hailar Basin. On this basis, we explore the formation environment and genetic mechanisms of siderite and the influence of siderite on the hydrocarbon generation of source rocks in petroliferous basins, aiming to provide a theoretical basis for oil and gas exploration in this area.

## 2. Geological Setting

The Hailar Basin is located at the junction of the Erguna block and the Xing'an block in the eastern Xingmeng orogenic belt. To the south, it is integrated with the Tamuchag Basin in northeastern Mongolia. The interior of the basin can be divided into five first-order structural units (three depressions and two uplifts), consisting of sixteen sags [35] (Figure 1a). The basement of the basin is composed of pre-Paleozoic and Paleozoic epimetamorphic rocks. The sedimentary strata of the basin are composed of Mesozoic (Jurassic and Cretaceous) and Cenozoic strata, totaling a thickness of approximately 6000 m. The Mesozoic stratum contains, from bottom to top, the Upper Jurassic Tamulangou Formation ( $J_3tm$ ), the Lower Cretaceous Tongbomia Formation ( $K_1t$ ), the Nantun Formation ( $K_1n$ ), the Damoguaihe Formation ( $K_1d$ ), the Yimin Formation ( $K_1y$ ), and the Qingyuangang Formation ( $K_2q$ ) [33,34,36,37] (Figure 1c). In this,  $J_3tm$  is interbedded with volcanic rocks and clastic rock;  $K_1t$  is mainly composed of sandstone and conglomerate.  $K_1n$  is composed of sand and mudstone interbedded in shallow lake facies;  $K_1d$  and  $K_1y$  are mainly composed of mudstone;  $K_2q$  is mainly composed of conglomerate. At present, oil and gas exploration in the Hailar Basin is mainly concentrated in the Wuertun and Beier sags, two oil-rich sags in the central fault zone. Breakthroughs in oil and gas exploration have been made in the Huhehu, Bayanhushu, and Hongqi sags in the Hailar basin, and good hydrocarbon indications have been found in the Yimin and Dongming sags. However, overall, no large-scale hydrocarbon reserves have been formed in the basin. The lacustrine source rocks of the Lower Cretaceous Nantun Formation in the Hailar Basin are dominated by dark mudstones. This set of source rocks has good hydrocarbon generation potential and is the main source rock series in the Hailar Basin. The Dongming sag (the study area) is in the northeastern Hailar Basin. It is a graben-shaped sag that is faulted in the south and overlapped in the north, with an area of 665 km<sup>2</sup>, showing a structural pattern of segmentation in the east–west direction and zonation in the south–north direction (Figure 1b). Well MD2 revealed that the first member of the Nantun Formation ( $K_1n^1$ ) contains multiple siderite beds.

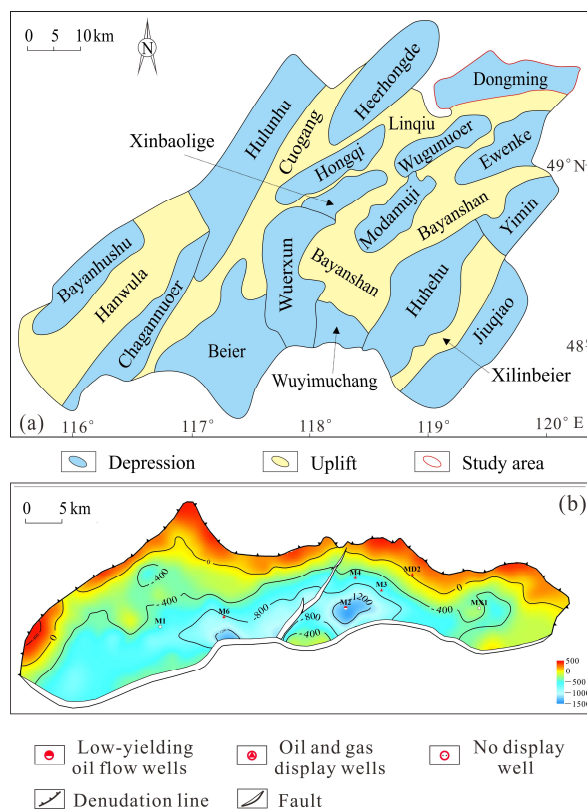


Figure 1. Cont.



southern steep slope zone, braided river delta deposits developed in the northern gentle slope zone, littoral shallow–semi-deep lacustrine deposits developed in the center of the lake basin, and sub-lacustrine fans developed locally. The strong tectonic subsidence led to the rise of the lake level. During this period, shore shallow lake semi-deep lake dark mudstone was deposited, which is the main source rock in the study area.  $K_1n^1$  in well MD2 is mainly made up of thick black-dark gray mudstone, containing sandstone, and siltstone bands with varying thicknesses.

### 3. Samples and Methods

In this study, gray-dark gray mudstone and gray-black silty mudstone cores and detrital samples were sampled in the Dongming sag. In total, 23 samples were subjected to total organic carbon determination, rock-eval analysis, Ro determination, and kerogen microcomponent analysis (Table 1). This experimental analysis was performed by the laboratory of the Institute of Organic Geochemistry, PetroChina Daqing Oilfield Co., Ltd., Daqing, China.

**Table 1.** TOC, Rock-Eval, and Ro data of the black mud and coal samples in Dongming Sag.

Well	Depth/m	Sample	TOC/%	Tmax/°C	(S <sub>1</sub> + S <sub>2</sub> )/(mg/g)	Ro/%
M2	2780.00	Coal chips	62.74	497.00	41.51	1.55
M3	1567.00	Coal chips	62.04	440.00	120.95	0.79
M3	1587.00	Coal chips	59.68	439.00	161.93	0.79
M3	1647.00	Coal chips	64.56	438.00	190.24	0.80
M3	1750.00	Mud	1.62	440.00	2.69	0.80
M3	1912.00	Coal chips	65.20	404.00	29.90	0.80
M3	2248.00	Mud	1.88	442.00	1.69	0.81
M3	2342.00	Mud	3.96	439.00	2.43	0.81
M3	1452.43	Coal	36.07	444.00	44.32	0.76
BD1	510.85	Mud	2.87	434.00	1.49	0.49
BD1	548.75	Coal	46.25	429.00	24.12	0.48
BD1	700.70	Mud	2.02	439.00	1.81	0.63
BD1	744.60	Mud	2.13	442.00	9.44	0.65
BD1	779.85	Mud	1.50	438.00	1.76	0.68
BD1	818.45	Mud	6.70	445.00	4.92	0.69
BD1	873.20	Mud	2.10	439.00	6.31	0.78
BD1	909.60	Mud	1.93	454.00	1.54	0.82
BD1	970.15	Mud	2.24	442.00	2.70	0.87
BD1	990.35	Mud	0.93	427.00	0.27	0.89
M1	557.06	Mud	2.48	429.00	2.45	0.46
M1	977.78	Mud	2.99	432.00	12.68	0.52
M1	1033.29	Mud	3.35	433.00	13.07	0.52
M1	1425.39	Mud	3.09	438.00	7.93	0.55

In addition, based on the observation of the whole-well core of well MD2, fresh core samples were collected from dark mudstone and siderite beds of the well in  $K_1n^1$  for systematic analysis of carbonate content, X-ray diffraction, major and trace element analysis, carbon and oxygen isotope analysis, thin-section analysis, scanning electron microscopy (SEM), cathodoluminescence, and energy-dispersive spectroscopy. Specifically, thin-section analysis and core description were used to observe the macromorphological and micromorphological characteristics of siderite. Elemental analysis and carbon and oxygen isotope analysis were used to identify the depositional paleoenvironment of the source rocks and siderite beds in  $K_1n^1$ . The above experimental analyses were all performed by the State Key Laboratory of Oil and Gas Reservoir Geology and Development, Chengdu University of Technology.

## 4. Experimental Results

### 4.1. Macroscopic Development Characteristics of Siderite Beds

Based on the core observation of well MD2, there are 23 siderite beds in the dark mudstone of  $K_1n^1$ , including 20 yellow-brown beds and 3 gray-brown beds (Figure 2a). From the logging curve, the anomalous values of the lower peak value in both GR and AC, but higher peak value in LLD are observed, which is the result of siderite enrichment. The macroscopic appearance of the siderite beds is similar to that of the mudstone beds, but the density of siderite is significantly higher than that of the surrounding mudstone. The thickness of a single siderite bed varies from 2 to 60 cm, and the cumulative thickness of siderite bed reaches 3.45 m. Dropping cold hydrochloric acid onto a siderite bed does not cause bubbling. The siderites in the mudstone are mostly irregular blocks, with a long axis almost parallel to the stratum and clear boundaries with the overlying and underlying surrounding rocks. Some siderites are lenticular, lamellar, or nodular, with unclear boundaries with the surrounding rocks (Figure 2b,d). Fractures filled with white bentonite can be observed in some siderite beds (Figure 2c). The characteristics of the siderite give important hints about its genetic mechanism, and stratiform or massive occurrence can be used as one of the hallmarks of authigenic siderite [4]. In addition, 10 well-stratified thin layers of tuff were observed in well MD2 (Figure 2e), with thicknesses ranging from 4 mm to 2 cm. These tuff layers coincide well with the strong regional volcanic activity during the depositional period of the  $K_1n^1$  of the Hailar Basin [38]. After the Early Jurassic (approximately 197 Ma), northeast China was in an extensional tectonic environment (mantle uplift, crust extension, and thinning) and had a high-temperature geological background (created by strong magmatic activity) due to the subduction of the Kura-Pacific plate and the extension and closure of the Okhotsk–Mohe–Mongolian Ocean [39]. During the Early Cretaceous, there were two periods of volcanism in the Hailar Basin: from the Late Jurassic to the early Early Cretaceous (152–138 Ma) and in the late Early Cretaceous (128–117 Ma) [40], depositing mainly rhyolite-fused tuff, sedimentary breccia, and sedimentary tuff, followed by tuffaceous conglomerate and sandstone, and a small amount of andesite and andesitic tuff [41].

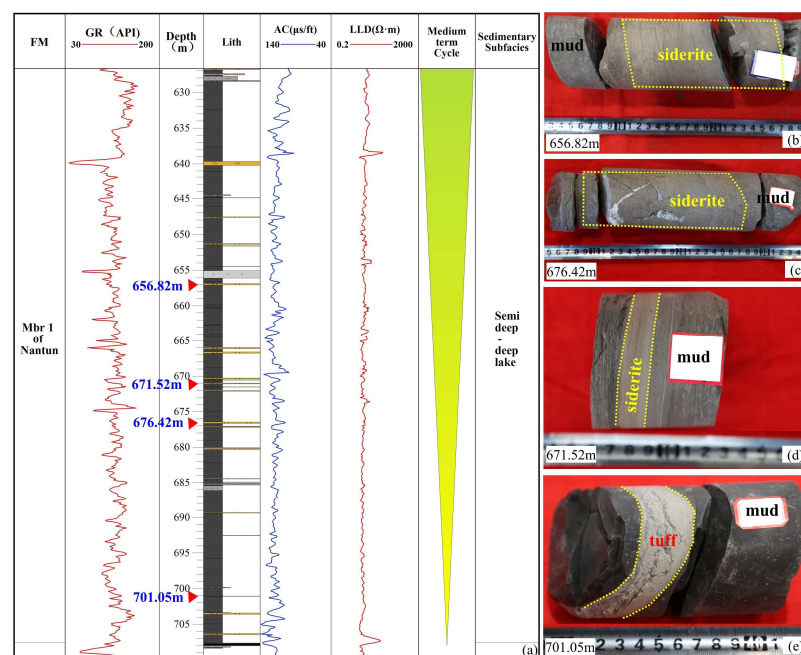


**Figure 2.** The stratigraphic profile of  $K_1n^1$  in well MD2 and photographs of typical siderite and tuff cores. (a) stratigraphic profile of  $K_1n^1$  in well MD2, including the location of (b–e); (b) lenticular siderite with unclear boundaries with the surrounding rocks; (c) fractures filled with white bentonite can be observed in some siderite beds; (d) layered siderite; (e) well-stratified thin layers of tuff.

#### 4.2. Micromorphological Characteristics of the Siderite Beds

The thin-section analysis and cathodoluminescence results of samples collected from well MD2 show that siderite appears yellow-brown under plane-polarized light and brown under cross-polarized light. According to its micromorphological characteristics, siderite can be divided into three occurrence forms: (1) dense micronized crystals with distinct crystal grains and associated calcite (Figure 3a); (2) banded distribution, two veins of calcite and siderite, and good stratification (Figure 3b); (3) paragenesis with quartz and calcite, an obvious Maltese-cross extinction pattern under cross-polarized light, and terrestrial plant debris observable under the microscope (Figure 3c,d). Under the SEM, clay mineral aggregates, charcoal, algal fossils, granular pyrite crystals, silicate bands, and other mineral types are observed in the siderite samples, which are intercalated with feldspar crystals, schistose mica, book-like kaolinite, and a few micropores (Figure 4).

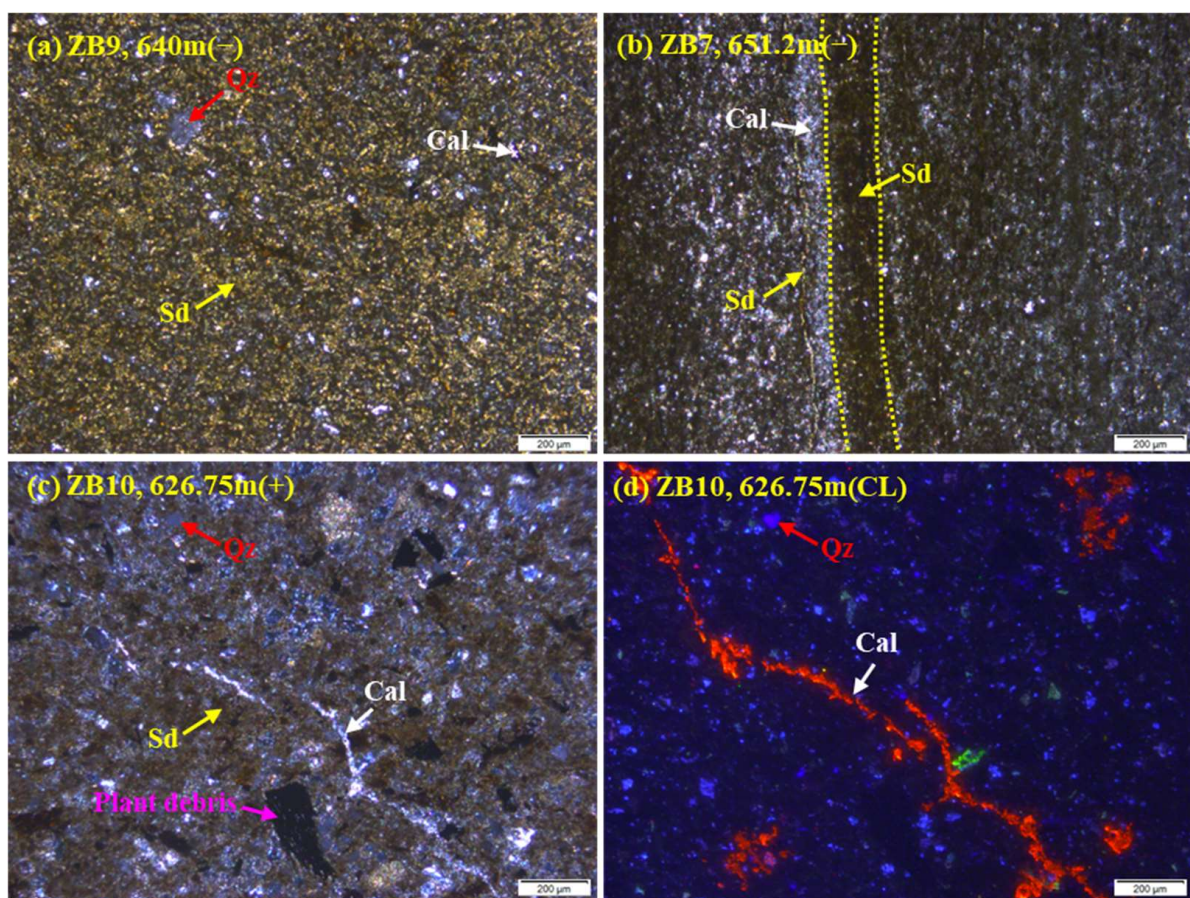


**Figure 3.** Microscopic lithofacies characteristics of the siderite beds in K<sub>1n</sub><sup>1</sup> in well MD2: (a) micronized crystals; (b) stratiform occurrence, replacement of calcite by siderite; (c,d) paragenesis with quartz and calcite and the presence of plant debris. Qz = quartz, Sd = siderite, Cal = calcite, CL = cathodoluminescence, (+) = cross-polarized light, (-) = plane-polarized light.

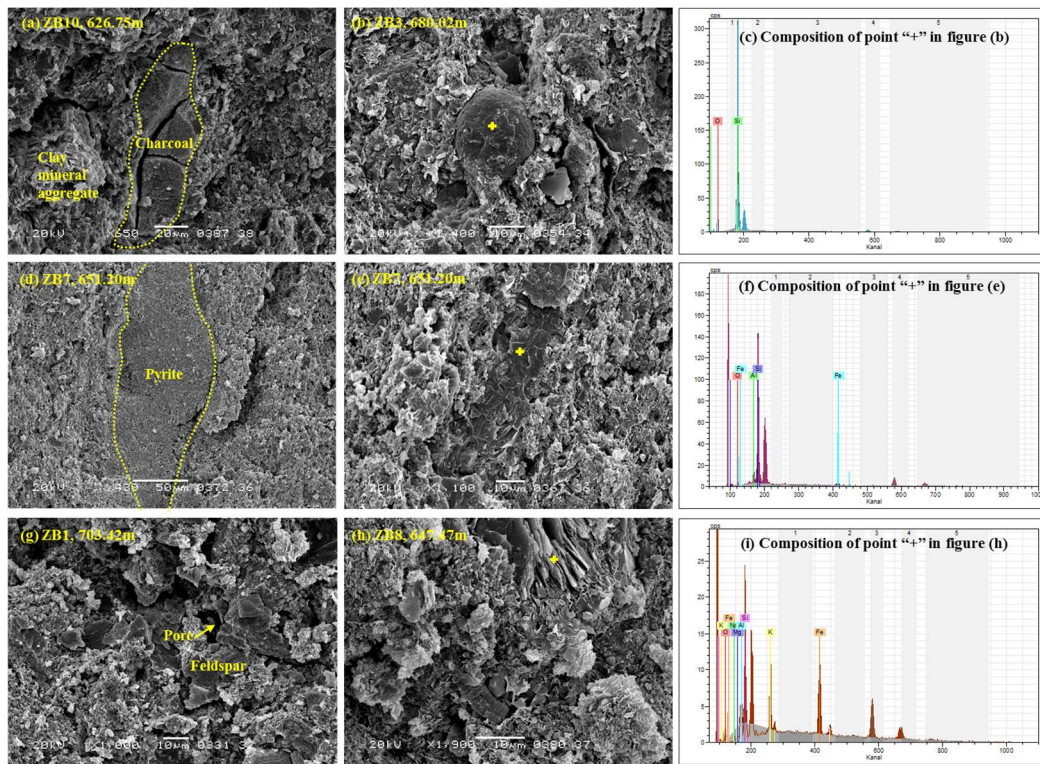


**Figure 4.** Mineral composition of the siderite beds in  $K_1n^1$  in well MD2: (a) charcoal suspended in siderite; (b) algal fossils interspersed with platelet clay minerals; (d) granular pyrite crystals in banded distribution; (e) quartz veinlets; (g) feldspar crystals and micropores; (h) interbeds of schistose mica and book-like kaolinite; “+” in (b,e,h) is the location of energy-dispersive spectra; (c,f,i) energy-dispersive spectra.

### 4.3. Petromineralogical Characteristics of Siderite Beds

To further understand the mineral composition of the deposits of  $K_1n^1$ , a total of 20 samples were collected from the mudstone, siltstone, sandy conglomerate, and siderite beds for X-ray diffraction analysis (Table 2). In addition to quartz, feldspar, and clay minerals, all mudstone samples collected from  $K_1n^1$  contain 2% to 10% siderite. The siltstone and sandy conglomerate samples do not contain siderite. The siderite samples have siderite as a main mineral component (content: 10% to 62%), followed by clay minerals, quartz, and feldspar, and two siderite samples are quartz-free (Figure 5a). Hou et al. [40] analyzed the minerals in  $K_1n^1$  in well MD2 and noted that the content of siderite in some beds reached 90% and that some samples contained a small amount of ankerite and pyrite.

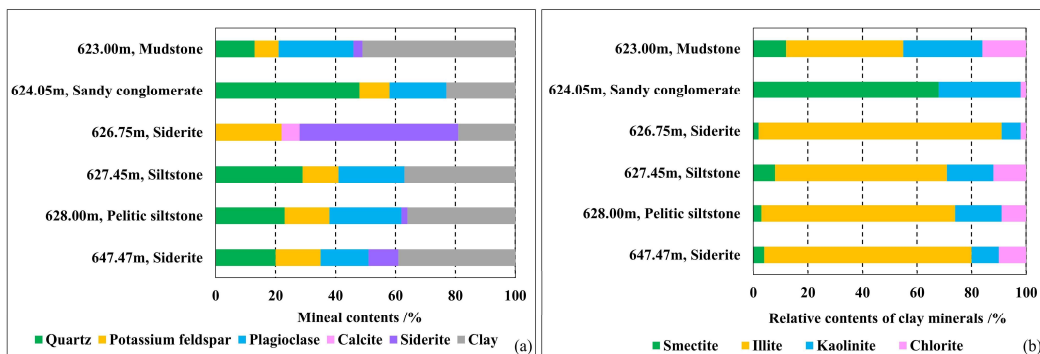


**Figure 5.** Mineral content (a) and relative content of clay minerals (b) measured using X-ray diffraction for different lithologies in  $K_1n^1$  in well MD2.

**Table 2.** Major element contents of the samples from well MD2.

Sample ID	Lith	Depth /m	Quartz /%	Feldspar /%	Plagioclase /%	Calcite /%	Dolomite /%	Siderite /%	Total Clay Content /%	Clay Minerals/%			
										Smectite	Illite	Kaolinite	Chlorite
Z38	Black mud	623.00	13.00	8.00	25.00			3.00	51.00	12.00	43.00	29.00	16.00
Z37	Siltstone	623.55	46.00	9.00	15.00				30.00	17.07		7.33	
Z36	Sandy conglomerate	624.05	48.00	10.00	19.00				23.00	68.00		30.00	
Z35	Sandy conglomerate	624.30	48.00	9.00	20.00				23.00	2.00		32.00	
Z33	Black mud	625.60	25.00	12.00	21.00			4.00	38.00	4.00	90.00	4.00	4.00
s12	Black mud	625.60	23.00	8.00	18.00			2.00	49.00	12.00	41.00	30.00	17.00
ZB10	Siderite	626.75		22.00		6.00		53.00	19.00	2.00	89.00	7.00	2.00
s11	Gray siltstone	627.45	29.00	12.00	22.00				37.00	8.00	63.00	17.00	12.00
Z31	Black mud	627.70	18.00	10.00	20.00			2.00	50.00	32.00	40.00	23.00	5.00
Z30	Siltstone	628.00	22.00	15.00	24.00			2.00	36.00	3.00	71.00	17.00	9.00
Z29	Black mud	629.05	26.00	17.00	19.00			3.00	35.00	7.00	43.00	44.00	6.00
s10	Black mud	631.10	25.00	15.00	19.00			3.00	38.00	5.00	70.00	13.00	12.00
s9	Black mud	634.77	26.00	15.00	22.00			2.00	35.00	13.00	36.00	51.00	
s41	Black mud	636.97	24.00	18.00	20.00			2.00	36.00	2.00	77.00	11.00	10.00
ZB9	Siderite	640.00		22.00		6.00		50.00	22.00	6.00	70.00	19.00	5.00
s39	Black mud	640.10	22.00	19.00	11.00			8.00	40.00	11.00	61.00	19.00	9.00
s40	Black mud	641.57	22.00	20.00	24.00			10.00	34.00	1.00	89.00	6.00	4.00
ZB8	Siderite	647.47	20.00	15.00	16.00			10.00	39.00	4.00	76.00	10.00	10.00
s38	Black mud	649.70	23.00	13.00	21.00			4.00	39.00	7.00	58.00	23.00	12.00
ZB1	Siderite	703.42	25.00					62.00	13.00	15.00	18.00	42.00	24.00

#### 4.4. Characteristics of Main and Trace Elements

The contents and related parameters of major and trace elements are shown in Tables 3 and 4. Major elements can be used to judge the original sedimentary fabric and the allochem percentage in sedimentary grains [42]. The oxides in the siderite beds in well MD2 include  $\text{Fe}_2\text{O}_3$  (highest proportion, 14.33% to 57.67%; mean: 43.79%),  $\text{SiO}_2$ ,  $\text{Al}_2\text{O}_3$ , and oxides of Ca, Na, K, and Mg (generally less than 1%). The dark mudstone mainly consists of  $\text{SiO}_2$  and  $\text{Al}_2\text{O}_3$  and generally contains less than 5% other oxides. The trace elements in the siderite beds are typically characterized by high Mn contents (which exceed 10,000  $\mu\text{g/g}$  in all but one sample). Because Mn has a tendency to be enriched in the mudstone, it is hypothesized that the same depositional period brought an adequate supply of Mn from terrestrial sources of debris, along with a stronger solubility in reducing waters. In addition, besides the Be content in siderite beds being slightly higher than that of dark mudstone, the contents of other elements in siderite beds are equivalent to or slightly lower than that of dark mudstone. Be is a high-temperature mineralizing element, and its enrichment has good mineralization specificity with igneous rocks. Due to the background of volcanic activity, Be enrichment is thought to be related to volcanism.

**Table 3.** Major element contents of the samples from well MD2.

Sample ID	Lith	Element Content/%									
		LOI	Carbonate	SiO <sub>2</sub>	Al <sub>2</sub> O <sub>3</sub>	CaO	TFe <sub>2</sub> O <sub>3</sub>	K <sub>2</sub> O	MgO	Na <sub>2</sub> O	CIA
Z27	Black mud	6.18	8.38	74.25	13.9	2.2	2.46	2.83	0.56	1.23	68.96
Z29	Black mud	5.04	5.83	73.35	15.81	0.79	1.62	5.13	0.49	1.66	67.58
Z30	Siltstone	8.01	10.32	60.42	20.48	2.31	4.54	2.56	1	2.23	74.27
Z31	Black mud	12.68	16.61	55.92	13.36	3.92	14.56	3.17	0.94	1.75	60.17
Z33	Black mud	7.35	8.52	63.56	20.06	1.18	4.07	3.59	0.74	2.04	74.65
Z35	Sandy conglomerate	8.73	10.02	64.3	18.27	1.29	3.99	3.27	0.68	1.66	74.59
Z36	Sandy conglomerate	5.55	10.01	76.8	13.67	4.46	2.05	4.82	0.42	2.03	54.72
Z37	Siltstone	7.5	8.61	66.75	17.82	1.12	2.96	3.11	0.75	1.69	75.05
Z38	Black mud	8.68	9.96	61.38	20.14	1.28	2.93	2.37	0.82	1.9	78.39
ZB1	Siderite	21.28	22.08	26.1	13.72	0.81	33.57	0.72	0.49	0.37	87.88
ZB2	Siderite	13.05	14.31	52	15.29	1.26	14.33	1.83	0.59	0.87	79.43
ZB3	Siderite	21.86	22.4	28.29	7.53	0.54	36.85	0.93	0.47	0.53	79.02
ZB4	Siderite	28.46	29.23	10.49	3.84	0.77	52.56	0.34	0.25	0.28	73.44
ZB5	Siderite	29.92	30.48	6.98	3.25	0.56	53.56	0.23	0.17	0.2	76.71
ZB6	Siderite	29.14	30.3	9.27	3.11	1.15	54.43	0.14	0.66	0.18	67.92
ZB7	Siderite	22.26	23.26	31.07	6.6	1	35.49	1.01	1.38	0.59	71.76
ZB8	Siderite	23.73	25.41	23.04	6.95	1.68	41.03	0.74	0.96	0.45	70.81
ZB9	Siderite	29.43	30.55	5.41	3.68	1.12	57.68	0.21	0.63	0.2	70.56
ZB10	Siderite	19.46	23.38	32.23	11.07	3.93	32.09	1.31	1.24	0.85	64.51
s15	Black mud	12.26	12.88	53.08	22.96	0.62	5.34	2.36	0.56	0.7	86.22
s14	Sandy mudstone	9.40	10.25	59.53	22.42	0.85	3.17	2.74	0.7	0.87	83.39
s1	Black mud	11.94	12.66	59.23	18.89	0.72	3.05	1.98	0.71	0.91	83.97
s3	Black mud	9.83	10.97	62.8	16.88	1.14	4.95	1.94	0.78	0.94	80.77
s4	Black mud	9.00	10.01	66.69	16.73	1.00	2.91	2.29	0.83	1.04	79.43
s5	Black mud	9.12	10.15	67.54	16.49	1.03	2.44	3.09	0.96	1.38	75
s6	Black mud	8.63	9.22	68.47	15.86	0.59	1.91	2.56	0.68	1.14	78.72
s8	Black mud	9.39	10.16	69.27	13.78	0.77	2.07	2.25	0.8	1.17	76.69
s10	Black mud	8.93	9.54	65.52	18.38	0.61	1.80	3.50	0.56	1.21	77.56
s11	Gray siltstone	9.13	9.96	63.55	18.07	0.83	2.39	2.81	0.77	1.49	77.88
s9	Black mud	9.56	10.01	65.03	18.28	0.46	2.05	3.41	0.58	1.3	77.95
s13	Black mud	10.89	11.55	57.44	21.53	0.66	3.12	1.75	0.54	0.79	87.1
s28	Black mud	9.83	11.57	60.1	21.04	1.74	2.8	1.93	0.59	0.87	82.26
s30	Black mud	9.65	10.83	64.38	17.59	1.17	2.82	2.44	0.87	1.26	78.32
s32	Black mud	8.54	9.09	67.42	16.23	0.55	2.76	2.27	0.66	1.07	80.66
s34	Black mud	40.6	40.92	43.35	6.6	0.32	0.75	0.84	0.19	0.42	80.71
s36	Gray mud	8.94	9.80	66.83	16.1	0.86	2.36	3.09	0.86	1.37	75.17
s29	Black mud	11.88	12.48	67.39	11.73	0.60	3.20	2.40	0.64	0.95	74.85
s31	Black mud	11.38	14.97	61.65	16.83	3.59	4.05	1.59	0.7	1.11	72.8
s35	Black mud	8.98	9.75	66.29	16.92	0.77	2.18	2.92	0.72	1.39	76.89
s37	Black mud	10.02	10.87	65.06	16.25	0.85	3.52	2.45	0.66	1.12	78.61
s38	Black mud	8.48	9.13	67.87	14.91	0.64	2.28	2.57	0.73	1.3	76.74
s39	Black mud	29.64	30.66	8.8	2.46	1.02	55.61	0.21	0.48	0.17	63.68

Note: Chemical index of alteration CIA =  $100 \times \text{Al}_2\text{O}_3 / (\text{Al}_2\text{O}_3 + \text{CaO} + \text{Na}_2\text{O} + \text{K}_2\text{O})$ .

**Table 4.** Trace element contents of the samples from well MD2.

Sample ID	Lith	Element Content/(10 <sup>-6</sup> µg g <sup>-1</sup> )																	
		Li	Be	Ti	Sc	V	Cr	Mn	Co	Ni	Cu	Zn	Rb	Sr	Zr	Ba	Pb	Th	U
ZB1	Siderite	26.51	5.24	2135.98	16.41	87.21	25.30	10,520.39	8.76	8.98	8.94	61.15	43.65	121.12	290.60	327.09	17.16	17.27	2.76
ZB2	Siderite	33.84	5.97	3294.97	10.03	83.73	33.72	7126.65	10.22	11.23	12.70	166.81	90.94	223.14	354.76	560.61	33.66	15.57	4.29
ZB3	Siderite	21.60	6.53	1482.99	6.13	100.35	20.69	16,159.48	6.25	6.84	4.55	43.22	40.48	106.35	212.80	376.61	12.09	6.57	1.98
ZB4	Siderite	13.55	5.61	781.79	4.13	50.15	23.96	24,242.81	3.77	4.95	4.57	63.12	17.62	63.87	97.49	260.73	6.77	4.06	0.90
ZB5	Siderite	13.28	1.63	646.49	2.63	15.90	16.00	44,902.11	1.78	3.85	7.48	13.77	12.85	60.82	78.48	259.40	2.12	3.09	0.76
ZB6	Siderite	11.71	8.74	490.80	4.93	72.20	20.87	24,762.04	2.03	3.73	3.74	21.11	9.04	45.77	82.59	165.28	10.85	3.20	0.67
ZB7	Siderite	16.35	6.55	1133.99	7.49	66.63	34.76	13,058.05	7.66	8.39	9.41	25.35	43.97	75.76	225.97	363.02	11.20	7.50	2.18
ZB8	Siderite	19.67	7.38	1459.99	5.54	61.67	22.62	17,625.92	6.68	8.04	5.62	52.84	31.25	91.78	225.40	289.46	15.18	7.29	2.25
ZB9	Siderite	11.35	3.86	614.29	3.01	29.83	23.55	20,802.19	1.83	3.81	4.92	23.21	12.45	108.90	99.08	339.61	8.86	3.74	0.96
s4	Black mud	41.71	3.59	3714.96	11.43	113.86	38.96	171.42	7.63	12.73	17.49	80.84	106.47	236.50	523.41	631.49	19.34	19.59	5.02
s5	Black mud	30.47	3.79	3186.97	13.09	112.77	36.32	139.90	9.45	14.30	19.74	51.58	143.32	197.75	491.49	599.69	23.46	20.18	4.95
s6	Black mud	36.98	3.42	3287.97	11.72	117.41	31.77	170.74	9.87	11.74	15.32	60.63	117.20	193.41	413.53	547.97	18.28	16.16	4.04
s11	Gray siltstone	35.71	3.35	4108.96	11.67	90.00	29.18	214.66	14.17	13.61	21.73	68.58	116.84	259.82	554.42	692.26	26.44	19.23	4.60
s28	Black mud	52.20	4.00	3548.97	14.20	100.79	28.14	261.89	12.05	12.88	14.37	88.98	99.33	268.99	613.34	573.70	29.75	25.00	5.40

Table 4. Cont.

Sample ID	Lith	Element Content/(10 <sup>-6</sup> μg·g <sup>-1</sup> )																	
		Li	Be	Ti	Sc	V	Cr	Mn	Co	Ni	Cu	Zn	Rb	Sr	Zr	Ba	Pb	Th	U
s30	Black mud	42.11	4.02	4221.96	13.20	114.52	39.07	175.35	14.08	16.83	21.14	125.20	116.44	278.42	612.22	736.60	22.18	21.32	5.49
s32	Black mud	37.93	3.56	3616.96	11.73	106.22	28.36	404.67	11.55	12.80	16.73	70.80	111.72	212.41	493.06	654.18	20.23	17.75	4.73
s34	Black mud	24.67	5.10	1556.98	4.12	32.58	18.87	92.24	2.82	4.85	7.70	21.67	37.38	83.75	210.01	252.94	5.08	8.61	2.29
s36	Gray mud	36.81	3.60	3671.96	12.98	116.57	41.43	342.01	13.22	14.52	17.35	100.18	140.96	254.12	506.00	708.89	26.15	18.90	5.04
s29	Black mud	31.22	3.58	3020.97	10.59	145.08	39.44	135.86	20.99	19.71	21.06	123.71	122.30	155.16	409.50	553.41	26.70	16.21	5.28
s38	Black mud	33.54	3.19	3193.97	11.31	98.35	30.23	273.72	6.98	9.82	16.05	72.79	117.70	212.67	445.68	628.28	22.27	16.69	4.42
s39	Black mud	10.37	2.49	579.90	2.25	21.61	18.38	21,865.95	1.85	4.16	5.50	21.78	12.57	92.30	83.60	311.33	6.87	3.26	0.80

#### 4.5. Characteristics of Carbon and Oxygen Isotopes

Table 5 shows the results of carbon and oxygen isotopes measured in this study. The carbonate minerals in the siderite beds are enriched with heavy carbon isotopes. The range of  $\delta^{13}\text{C}_{\text{v-PDB}}$  (−0.20–1.11‰; mean: 0.62‰) is narrow, while the range of  $\delta^{18}\text{O}_{\text{v-PDB}}$  (−18.22‰ to −10.14‰; mean: −14.23‰) is wide. Compared with the siderite beds, the dark mudstone exhibits lighter carbon isotopic compositions (−1.98 to −3.28‰) and heavier oxygen isotopic compositions (−7.59 to −10.25‰).

Table 5. Carbon and oxygen isotope data of the Mbr 1 of the Nantun formation from well MD2.

Sample ID	Lith	Depth/m	$\delta^{13}\text{C}_{\text{‰}} (\text{V}_{\text{PDB}})$		$\delta^{18}\text{O}_{\text{‰}} (\text{V}_{\text{PDB}})$	
			Measured Value	Standard Deviation	Measured Value	Standard Deviation
Z27	Black mud	655.97	−3.28	0.10	−10.25	0.30
Z30	Gray silty mudstone	628.00	−1.98	0.08	−7.59	0.03
ZB1	Siderite	703.42	0.99	0.07	−16.53	0.05
ZB3	Siderite	680.02	1.02	0.06	−12.33	0.04
ZB5	Siderite	670.47	1.11	0.07	−13.45	0.06
ZB7	Siderite	651.20	0.89	0.08	−14.86	0.05
ZB9	Siderite	640.00	−0.20	0.03	−10.14	0.30
ZB10	Siderite	626.75	−0.10	0.06	−18.12	0.20

## 5. Discussion

### 5.1. Restoration of the Paleoenvironment during the Depositional Period of $K_1n^1$

Sr and Ba contents and Sr/Ba ratios can be used to qualitatively reflect paleosalinity [42–47]. Generally, the concentration of Sr in saltwater is 800–1000 μg/g, and the concentration of Sr in fresh water is 100–300 μg/g. Sr/Ba > 1.0 indicates a saltwater (marine, saline lacustrine) medium; Sr/Ba < 0.6 indicates a terrestrial freshwater medium; and Sr/Ba between 0.6 and 1.0 indicates transitional brackish water deposits [46,47]. The Sr/Ba ratios of the siderite beds in well MD2 are 0.21–0.40 (mean: 0.29), and the Sr/Ba ratios of the dark mudstone are 0.28–0.38 (mean: 0.34). This suggests that the water in the lake basin was fresh water during the depositional period of  $K_1n^1$ .

As a redox-sensitive element, Ni is often precipitated in the form of sulfide under anoxic conditions and dissolved under oxidative conditions [44,46,48]. Elements such as U, V, and Cr in the depositional environment are easily soluble in oxidative conditions, insoluble in reducing environments, authigenically enriched in oxygen-deficient environments, and hardly migratable during diagenesis [38]. Th/U > 1.30 and V/Cr > 4.25 indicate a strong reducing environment, 0.8 < Th/U < 1.30 and 2.00 < V/Cr < 4.25 indicate a weak reducing environment, and Th/U < 0.8 and V/Cr < 2 indicate an oxidizing environment. The Th/U and V/Cr ratios of the siderite beds in well MD2 range from 3.25 to 6.25 (mean: 4.13) and from 0.99 to 4.85 (mean: 2.85), respectively. The Th/U and V/Cr ratios of dark mudstone range from 3.07 and 4.18 (mean: 3.84) and from 1.18 to 3.74 (mean: 2.92), respectively. Both the Th/U and V/Cr ratios of the two types of rocks indicate a reducing environment.

Under relatively stable tectonic conditions, climatic conditions control the temperature, pH, and paleosalinity of the depositional environment [47]. In this study, the chemical index of alteration (CIA) was used to judge the degree of chemical weathering and paleoclimate in the source area [47]. A CIA value between 50 and 65 ( $50 < CIA < 65$ ) indicates weak chemical alteration, a CIA value between 65 and 85 ( $65 < CIA < 85$ ) indicates moderate chemical alteration, and a CIA value between 85 and 100 ( $85 < CIA < 100$ ) indicates strong chemical alteration:

$$CIA = 100 \times Al_2O_3 / (Al_2O_3 + CaO^* + Na_2O + K_2O) \quad (1)$$

The CIA values of the siderite beds in well MD2 range from 64.50 to 79.42 (mean: 74.20), and the CIA values of the dark mudstone range from 54.72 to 87.10 (mean: 76.05). These results indicate that the chemical weathering during this period was moderate to strong and that the climate was semiarid to humid.

The Al/Ti ratios of the siderite beds and dark mudstone are both low, ranging from 0.20 to 0.34. Low Al/Ti ratios may indicate the input of a large amount of terrigenous detritus into the water bodies in the lake basin from faraway sources and the lake basin overall being in a relatively deep-water environment. In addition, the fractures developed in the siderite beds are filled with white bentonite. The magnesium-rich alkaline medium is an indispensable condition for the generation and maintenance of bentonite, whereas the exogenous alkaline medium, the warm and humid paleoclimate, and the formation of humic acid due to mass reproduction of plants cause silicate minerals (feldspar, mica, etc.) to release alkali metal ions, resulting in a weakly alkaline aqueous medium [49]. Therefore, the presence of bentonite reflects the warm and humid paleoclimate at that time.

In summary, the deposits of  $K_1n^1$  were formed in the depositional environment of a freshwater lake basin with deep water bodies.

## 5.2. Characteristics of Carbon and Oxygen Isotopes in Siderite Beds and Identification of Carbon Sources

Theoretically, enough  $Fe^{2+}$  and  $CO_3^{2-}$  is the prerequisite for siderite formation. The  $\delta^{13}C_{V-PDB}$  values of terrestrial lacustrine organic matter in Cretaceous or older sediments are approximately  $-25\%$  to  $-24\%$  [49], and the  $\delta^{13}C_{V-PDB}$  values of atmospheric freshwater, atmospheric  $CO_2$ , and carbonate deposits are  $-4\%$  to  $-1\%$ , approximately  $-7\%$ , and approximately  $0\%$ , respectively [24,49]. The  $\delta^{18}O_{V-PDB}$  values of natural oxygen compounds, atmospheric  $O_2$ , and atmospheric  $CO_2$  are approximately  $-55\%$  to  $-11\%$ ,  $-25\%$  to  $-22\%$ , and  $-42\%$  to  $-40\%$ , respectively. The oxygen isotope compositions of water in lakes ( $\delta^{18}O_{water}$ ) are mainly controlled by local precipitation from both rain and snowfall, inflowing water from both rivers and groundwater, and evaporation [50,51]. The  $\delta^{18}O$  of precipitating carbonates depends on the temperature of formation and the isotopic composition of the water. The  $\delta^{18}O$  value has a positive dependence of approximately  $0.28\% / ^\circ C$  [52]. Relatively light oxygen isotopic compositions indicate freshwater characteristics. Compared with the dark mudstone, the siderite beds in the deposits of  $K_1n^1$  have a distinct heavy carbon isotopic composition, which is similar to that of lacustrine carbonate (Figure 6) and is hardly affected by the  $HCO_3^-$  released by organic matter degradation. These findings indicate that the siderite beds formed in a deep-water, strongly reducing environment. The sources of  $CO_2$  in crustal fluids include sedimentary organic matter, carbonates, and magma–mantle [46]. There are two main sources of organic carbon in lacustrine sediments: one is the terrestrial organic debris brought by water flowing into lake basins, and the other is the aquatic organisms in lakes.  $K_1n^1$  is composed of thick, dark mudstone beds deposited against the background of a lake level rise. In addition, the atmospheric  $CO_2$  concentration was high during the depositional period, which dissolved in lake water to form  $HCO_3^-$ , making for a  $CO_2$  (atmosphere)– $HCO_3^-$  (solution)/ $CO_3^{2-}$  (carbonate) homeostasis system. According to the carbon and oxygen isotopic characteristics of the siderite beds in the study area, the source of  $CO_3^{2-}$  for the formation of siderite

might be mainly related to the dissolution of authigenic carbonates in the basin and the exchange of CO<sub>2</sub> between the atmosphere and lake water.

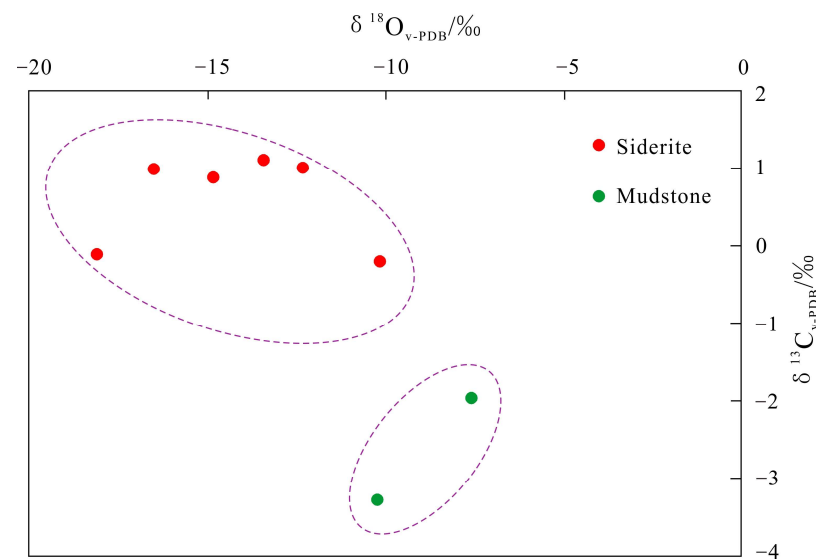


**Figure 6.**  $\delta^{13}\text{C}_{\text{v-PDB}}-\delta^{18}\text{O}_{\text{v-PDB}}$  diagram of the carbonate minerals in well MD2.

### 5.3. Genetic Mechanism of Siderite

Xie et al. [4] believed that stratiform or massive siderites may be authigenic or early-diagenetic. The siderite beds in the study area have a carbon isotopic composition close to that of the lacustrine carbonates, which is not affected by the degradation of sedimentary organic matter, so the siderite in the first member of the Lower Cretaceous Nantun Formation ( $K_1n^1$ ) of the Dongming sag, Hailar Basin, was authigenic in a deep-water lacustrine reducing environment. The Cretaceous was one of the typical greenhouse periods in geological history, in which the paleoclimate strongly controlled the development and distribution of paleontological groups and sediment types [18,19,53]. Notably, the Early Cretaceous was in a process of overall warming, the temperature peaking in the mid-Cretaceous. The Cretaceous greenhouse climate might be closely related to the high atmospheric CO<sub>2</sub> concentrations [53–55], which were 2 to 4 times higher than the current atmospheric CO<sub>2</sub> concentrations [53], and the temperature at that time was higher than the current temperature [54–57]. As an important environmental indicator mineral, siderite is usually formed in closed and anoxic lacustrine environments with relatively weak hydrodynamic conditions. The provenance of the Dongming sag in the Hailar Basin mainly comes from the southern steep slope and the northern gentle slope zone. The northern gentle slope zone has developed braided river delta deposits, with inputs of terrigenous detritus from faraway sources. During transportation, its Fe was oxidized to Fe<sup>3+</sup> by weathering, then transported through surface runoff and rivers, enriched in lake areas with weak hydrodynamics, and buried in the form of Fe(OH)<sub>3</sub> along with the organic matter deposited on the bottom of the lake. The warm and humid climate was suitable for plant growth, the vegetation around the lake basin was prosperous, and a large amount of greenhouse gases such as CO<sub>2</sub> were dissolved in lake water, which further promoted chemical weathering. The increased supply of various mineral elements accelerated the formation of authigenic minerals. Furthermore, during the depositional period of  $K_1n^1$ , the lake basin subsided rapidly, and the lake water level rose continuously. The warm lake water was conducive to the growth of organisms and the decay of organic matter, resulting in a sharp increase in oxygen consumed by the lake. After the volcanic eruption, the ash fell in the lake basin, which had the effect of increasing nutrients, not only made the microorganisms in the water body grow wildly in a short period of time, but also increased the salinity of the water body, resulting in the formation of stratification of the water body and bottom reduction

environment [58,59]. The increased oxygen consumption and the anoxic water environment jointly promoted the formation of the reducing lacustrine environment. When the supply of  $\text{Fe}^{3+}$  is high enough, organic matter reduces  $\text{Fe}^{3+}$  to  $\text{Fe}^{2+}$ , and the dissolution of carbonate and atmospheric  $\text{CO}_2$  can provide abundant  $\text{CO}_3^{2-}$  for the formation of siderite. Under these conditions,  $\text{Fe}^{2+}$  combines with  $\text{CO}_3^{2-}$  to form siderite (Figure 7).

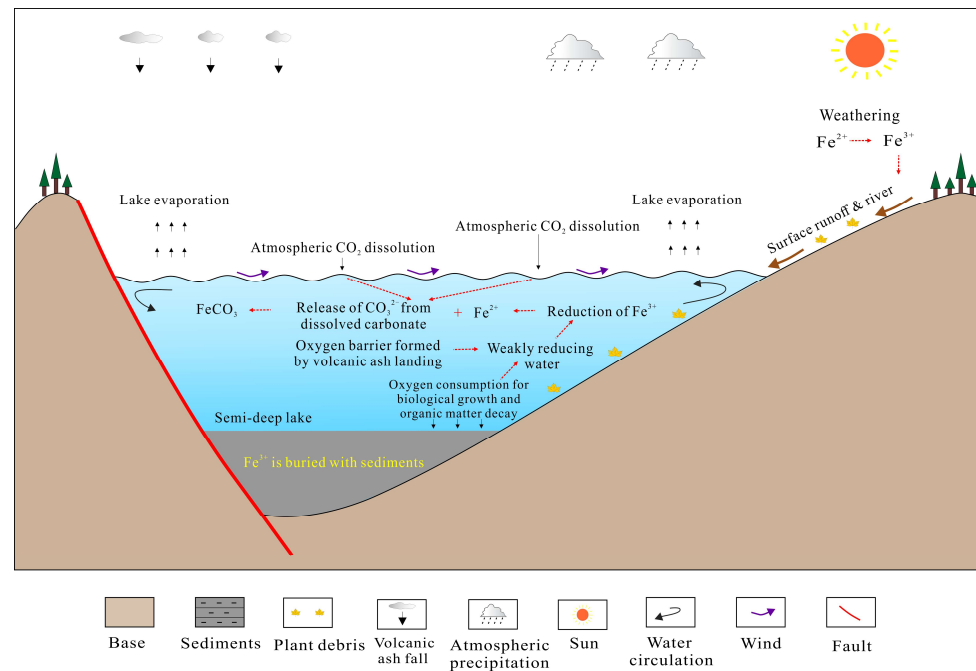


**Figure 7.** Conceptual model of siderite formation in  $K_1n^1$  of the Dongming sag.

#### 5.4. Discussion on the Relationship between Siderite and Source Rocks

The geochemical analysis of the source rocks in  $K_1n^1$  of the study area showed that the total organic carbon of the mud-source rocks of  $K_1n^1$  is 0.93% to 6.70% (mean: 2.61%). The potential of hydrocarbon generation ( $S_1 + S_2$ ) is 0.27 to 13.07 mg/g (mean: 4.57 mg/g). The kerogen is mainly of type II [58]. Microscopic examination showed algal fossils, sporophyte fossils, and vitrinites. The hydrocarbon source material is mainly from terrestrial higher plants. According to the Geochemistry Evaluation Method for Land Facies Hydrocarbon Source Rock (SY/T 5735-1995), this set of source rocks has high organic matter abundance and high hydrocarbon generation potential. The conventional geochemical characteristics and the depositional paleoenvironment indicated by the siderite evince excellent organic matter storage conditions and high hydrocarbon generation potential. Zhang et al. [33,34] concluded that the presence of siderite can promote the pyrolysis of organic matter in source rocks by increasing the pyrolysis rate and decreasing the temperature at which most organic matter is pyrolyzed by reducing the activation energy of the pyrolysis of organic matter. Compared with the source rocks with no siderite deposits in the Hongqi and Yimin sags of the Hailar Basin, the source rocks in  $K_1n^1$  of the Dongming sag in the study area have higher main frequency activation energy to generate liquid hydrocarbons [60]. Preliminary analysis suggested that this may be related to the selection of kerogen samples for the simulation of hydrocarbon generation kinetics without considering the influence of mineral components such as siderite on the kerogen.

#### 5.5. Recommendation for Future

Therefore, regarding the relationship between siderite and source rocks in the study area, there are still three issues that need to be studied and explored in depth. First, thin layers of tuff were found in the dark mudstone in the study area, but whether regional volcanic activity was involved in the formation of siderite beds, that is, whether the

source of Fe in siderite was related to magma, needs further confirmation. Second, since the diagenesis related to the complex process of siderite formation occurs at the same temperature as the transformation temperature of organic matter into hydrocarbons [34–36], siderite has a certain influence on the process, stage, mechanism, and scale of hydrocarbon generation. However, the underlying mechanism needs further theoretical exploration. Third, regional comparative studies are needed to clarify whether there are differences in the hydrocarbon generation potential and evolution of source rocks with and without siderite and whether the presence of siderite can be used as a sign of the presence of high-quality source rocks.

## 6. Conclusions

1. The siderites in  $K_1n^1$  are mostly stratiform or massive in the cores. There are three micromorphological features: dense micronized crystals, bands, and paragenesis with quartz and calcite, respectively. As the main mineral, the content of siderite exceeds 50%, followed by clay minerals, quartz, and feldspar. Under the microscope, a variety of mineral types, such as charcoal, algal fossils, granular pyrite crystals, and vein-like siliceous bands, were observed, which were intercalated with feldspar crystals, schistose mica, book-like kaolinite, and a small number of micropores.
2. The oxides in the siderite beds include  $Fe_2O_3$  (highest proportion),  $SiO_2$ ,  $Al_2O_3$ , etc. The trace elements were characterized by a high Mn and Be contents; low Sr/Ba, Th/U, and Al/Ti ratios; and high V/Cr ratios. This indicates that the study area was a semiarid–humid, weakly reducing, freshwater depositional paleoenvironment during the depositional period of  $K_1n^1$ .
3. The siderite has distinct characteristics of heavy carbon and light oxygen isotopic compositions, which are similar to the characteristics of carbon and oxygen isotopes of lacustrine carbonate and atmospheric  $CO_2$ . Hence, the carbon required for siderite formation mainly came from dissolution of carbonates and atmospheric  $CO_2$ .
4. In the dynamic equilibrium system of  $CO_2$  (atmosphere) and  $HCO_3^-$  (solution)/ $CO_3^{2-}$  (carbonate) in water bodies of the lake basin, the Fe supplied by the source area underwent physical and chemical weathering. When the resultant  $Fe^{2+}$  concentration reached saturation, authigenic siderite was formed when  $Fe^{2+}$  combined with  $CO_3^{2-}$ .

**Author Contributions:** Conceptualization, M.X. and F.M.; methodology, M.X., G.C. and C.Z.; validation, M.X., G.C. and C.Z.; formal analysis, M.X.; investigation, X.Z.; data curation, R.X.; writing—original draft preparation, M.X.; writing—review and editing, M.X. and X.Z.; supervision, C.Z.; project administration, F.M. All authors have read and agreed to the published version of the manuscript.

**Funding:** This work was supported by the National Natural Science Foundation of China [grant number 42072119]; and Science and Technology Project of PetroChina [grant number 101017kt1604003x20].

**Data Availability Statement:** The authors confirm that the data supporting the findings of this study are available within the article.

**Acknowledgments:** The authors are indebted to all reviewers for their insightful comments and suggestions, which have significantly improved the manuscript. The authors are very grateful to Daqing Oilfield Exploration and Development Research Institute, PetroChina, for their data support.

**Conflicts of Interest:** The authors declare no conflict of interest.

## References

1. Ohmoto, H.; Watanabe, Y.; Kumazawa, K. Evidence from massive siderite beds for a  $CO_2$ -rich atmosphere before ~1.8 billion years ago. *Nature* **2004**, *429*, 395–399. [[CrossRef](#)] [[PubMed](#)]
2. Bekker, A.; Slack, J.F.; Planavsky, N.; Krapez, B.; Hofmann, A.; Konhauser, K.O.; Rouxel, O.J. Iron formation: The sedimentary product of a complex interplay among mantle, tectonic, oceanic, and biospheric processes. *Econ. Geol.* **2010**, *105*, 467–508. [[CrossRef](#)]
3. Wittkop, C.; Teranes, J.; Lubenow, B.; Dean, W.E. Carbon- and oxygen-stable isotopic signatures of methanogenesis, temperature, and water column stratification in Holocene siderite varves. *Chem. Geol.* **2014**, *389*, 153–166. [[CrossRef](#)]

4. Xie, B.Z.; Sun, L.F.; Fang, H.; Shi, X.Y.; Tang, D.J. Siderite in banded iron formation of the Neoproterozoic Baizhiyan Formation, Shanxi Province: Genesis and palaeoenvironmental implications. *J. Palaeogeogr.* **2021**, *23*, 175–190. [[CrossRef](#)]
5. Frederichs, A.T.; Dobeneck, T.V.; Bleil, U.; Dekkers, M.J. Towards the identification of siderite, rhodochrosite, and vivianite in sediments by their low-temperature magnetic properties. *Phys. Chem. Earth Parts A/B/C* **2003**, *28*, 669–679. [[CrossRef](#)]
6. Dill, H.G. The “chessboard” classification scheme of mineral deposits: Mineralogy and geology from aluminum to zirconium. *Earth-Sci. Rev.* **2010**, *100*, 1–420. [[CrossRef](#)]
7. Ward, C.R. Analysis and significance of mineral matter in coal seams. *Int. J. Coal Geol.* **2002**, *50*, 135–168. [[CrossRef](#)]
8. Ward, C.R. Analysis, origin and significance of mineral matter in coal: An updated review. *Int. J. Coal Geol.* **2016**, *165*, 1–27. [[CrossRef](#)]
9. Johnson, C.M.; Ludois, L.M.; Beard, B.L.; Beukes, N.J.; Heimann, A. Iron formation carbonates: Paleooceanographic proxy or recorder of microbial diagenesis? *Geology* **2013**, *41*, 1147–1150. [[CrossRef](#)]
10. Köhler, I.; Konhauser, K.O.; Papineau, D.; Bekker, A.; Kappler, A. Biological carbon precursor to diagenetic siderite with spherical structures in iron formations. *Nat. Commun.* **2013**, *4*, 1741. [[CrossRef](#)]
11. Zhang, K.; Zhu, X.K. Genesis of siderites in the Xiamaling formation of Jixian section and its paleoceanic significance. *Acta Geol. Sin.* **2013**, *87*, 1430–1438.
12. Milesi, V.; Guyot, F.; Brunet, F.; Richard, L.; Recham, N.; Benedetti, M.; Dairou, J.; Prinzhofer, A. Formation of CO<sub>2</sub>, H<sub>2</sub> and condensed carbon from siderite dissolution in the 200–300 °C range and at 50MPa. *Geochim. Cosmochim. Acta* **2015**, *154*, 201–211. [[CrossRef](#)]
13. Milesi, V.; Prinzhofer, A.; Guyot, F.; Benedetti, M.; Rodrigues, R. Contribution of siderite–water interaction for the unconventional generation of hydrocarbon gases in the Solimões basin, north-west Brazil. *Mar. Pet. Geol.* **2016**, *71*, 168–182. [[CrossRef](#)]
14. Wang, N.; Dai, S.; Nechaev, V.P.; French, D.; Graham, I.T.; Zhao, F.; Zuo, J. Isotopes of carbon and oxygen of siderite and their genetic indications for the Late Permian critical-metal tuffaceous deposits (Nb–Zr–REY–Ga) from Yunnan, southwestern China. *Chem. Geol.* **2022**, *592*, 120727. [[CrossRef](#)]
15. Tu, G. *Collection of Tu Guangchi’s Academic Works*; Science Press: Beijing, China, 2010.
16. Zhang, Y.J.; Shen, Y.L.; Yang, T.Y.; Zhao, Y.; Tong, G.C. Development characteristics of siderite in the constraint of sequence frame: A case study of Late Permian coal measures in Panguan area. *J. China Coal Soc.* **2020**, *45*, 976–985. [[CrossRef](#)]
17. Chen, Z.; Yu, J.; Hou, K. Genesis of siderite in Xuanlong area in northwest Hebei province. *Chin. J. Geol.* **1982**, *17*, 395–402.
18. Liu, J.; Liu, J.; Gu, X. Basin fluids and their related ore deposits. *Acta Petrol. Mineral.* **1997**, *16*, 54–65.
19. Liu, M.; Chen, Z.; Chen, Q. The role of organic matter in the genesis of siderite from the Xuanlong area. *Acta Sedimentol. Sin.* **1997**, *15*, 98–104. [[CrossRef](#)]
20. Dill, H.G. A geological and mineralogical review of clay mineral deposits and phyllosilicate ore guides in Central Europe—A function of geodynamics and climate change. *Ore Geol. Rev.* **2020**, *119*, 103304. [[CrossRef](#)]
21. Siehl, A.; Thein, I. Minette-type ironstones. *Br. Geol. Soc. Spec. Publ.* **1989**, *46*, 175–193. [[CrossRef](#)]
22. Burkhalter, R.M. Ooidal ironstones and ferruginous microbialites: Origin and relation to sequence stratigraphy (Aalenian and Bajocian, Swiss Jura mountains). *Sedimentology* **1995**, *42*, 57–74. [[CrossRef](#)]
23. Santelli, C.M.; Welch, S.A.; Westrich, H.R.; Banfield, J.F. The effect of Fe-oxidizing bacteria on Fe-silicate mineral dissolution. *Chem. Geol.* **2001**, *180*, 99–115. [[CrossRef](#)]
24. Shen, Y.; Qin, Y.; Li, Z.; Jin, J.; Wei, Z.H.; Zheng, J.; Zhang, T.; Zong, Y.; Wang, X. The sedimentary origin and geological significance of siderite in the Longtan Formation of western Guizhou Province. *Earth Sci. Front.* **2017**, *24*, 152–161. [[CrossRef](#)]
25. Yang, X.; Zhang, X. The genesis of Ediacaran siderite-rich iron formations in North Qilian, and its constraints on ancient oceanic conditions. *Chin. Sci. Bull.* **2021**, *66*, 3032–3044. [[CrossRef](#)]
26. Huang, Y.; Wang, C. Progress of reactive iron burial in the marine and terrestrial sediments with its implications to the genesis of source rock in Songliao Basin. *Chin. J. Nat.* **2015**, *37*, 79–85.
27. Tannenbaum, E.; Kaplan, I.R. Low-Mr hydrocarbons generated during hydrous and dry pyrolysis of kerogen. *Nature* **1985**, *317*, 708–709. [[CrossRef](#)] [[PubMed](#)]
28. Tannenbaum, E.; Huizinga, B.J.; Kaplan, I.R. Role of minerals in thermal alteration of organic matter-II: A material balances. *AAPG Bull.* **1986**, *70*, 1156–1165. [[CrossRef](#)]
29. Zhao, W.Z.; Wang, Z.Y.; Wang, H.J.; Zecheng, W.; Shuichang, Z.; Wang, Z.; Zhang, Q.C. Cracking conditions of oils existing in different modes of occurrence and forward and backward inference of gas source rock kitchen of oil cracking type. *Geol. China* **2006**, *33*, 952–965.
30. Cai, Y.; Zhang, S.; He, K.; Mi, J.; Zhang, W.; Wang, X.; Wang, H.; Wu, C. Effects of inorganic minerals in source rocks on hydrocarbon generation from organic matter. *Pet. Geol. Exp.* **2017**, *39*, 253–260. [[CrossRef](#)]
31. Jin, Z.; Yuan, G.; Cao, Y.; Liu, K.; Wang, Y.; Sun, J.; Hao, X.; Zhou, L.; Wei, Y.; Wu, S. Interactions between hydrocarbon-bearing fluids and calcite in fused silica capillary capsules and geological implications for deeply-buried hydrocarbon reservoirs. *Sci. China Earth Sci.* **2022**, *65*, 299–316. [[CrossRef](#)]
32. Nigam, A.N.; Tripathi, R.P.; Singh, H.S.; Gambhir, R.S. Source rock evaluation of some wells in Jaisalmer Basin (India) using Mössbauer spectroscopy. *Fuel* **1991**, *70*, 262–266. [[CrossRef](#)]

33. Zhang, X.; Jia, Z.; Li, J.; Hou, Y.; Peng, W.; Zhang, H.; Chen, H.; Shen, W.; Liu, Z.; Chen, H. Controlling action of the tectonic evolution on the hydrocarbon accumulation in Hongqi Sag of Hailar Basin. *Pet. Geol. Oilfield Dev. Daqing* **2019**, *38*, 117–125. [[CrossRef](#)]
34. Zhang, Y.; Zhou, S.; Li, J.; Ma, Y.; Li, Y.; Chen, K.; Zhang, C.; Sun, Z. Effect of siderite on pyrolysis of organic matters in source rocks. *Geochimica* **2019**, *48*, 502–510. [[CrossRef](#)]
35. Meng, Q.A.; Wan, C.B.; Zhu, D.F.; Zhang, Y.L.; Ge, W.C.; Wu, F.Y. Age assignment and geological significance of the “Budate Group” in the Hailar Basin. *Sci. China Earth Sci.* **2013**, *56*, 970–979. [[CrossRef](#)]
36. Feng, Z.; Zhang, X.; Ren, Y.; Wu, H.; Li, C.; Dong, W. Hydrocarbon reservoir forming characteristics and distribution rule of Hailar Basin. *Pet. Geol. Oilfield Dev. Daqing* **2004**, *23*, 16–19.
37. Chen, G.; Li, J.; Wu, H.; Peng, W.; Li, J.; Xie, M.; Zhang, B.; Shi, X. Sedimentary characteristics, identification mark and formation mechanism of the slumping deepwater gravity flow in fault lacustrine basin: A case study on the consecutive coring Well of Ming D2 in Dongming sag, Hailar Basin. *Acta Pet. Sin.* **2018**, *39*, 1119–1129.
38. Hou, Y.; Ren, Y.; Li, S.; Zhang, H.; Wu, H.; Peng, W.; Li, J. Analysis of Cretaceous sedimentary characteristics and environment from well MD2 in Dongming depression, Hailar Basin. *Glob. Geol.* **2020**, *39*, 332–343.
39. Cui, J.; Zhao, J.; Ren, Z.; Jin, W.; Xing, L.; Wang, Y. Geochemical characteristics of lower cretaceous source rocks and thermal history in the Huhehu Depression, Hailar Basin. *Earth Sci.* **2020**, *45*, 238–250.
40. Chen, C.; Gao, Y.; Wu, H.; Qu, X.; Liu, Z.; Bai, X.; Wang, P. Zircon U-Pb chronology of volcanic rocks in the Hailar basin, NE China and its geological implications. *Earth Sci.* **2016**, *41*, 1259–1274.
41. Wang, H.; Liu, L.; Gao, Y.; Zhang, X. Discussion of diageneses of volcanoclastic rocks of Nantun Formation in Beier sags, Hailar Basin. *Glob. Geol.* **2005**, *24*, 219–224.
42. Fan, Q.; Fan, T.; Li, Y.; Zhang, J.; Gao, Z.; Chen, Y. Paleo-environments and development pattern of high-quality marine source rocks of the early Cambrian, Northern Tarim platform. *Earth Sci.* **2020**, *45*, 285–302. [[CrossRef](#)]
43. Deng, H.; Qian, K. *Sedimentary Geochemistry and Environmental Analysis*; Gansu Science and Technology Press: Lanzhou, China, 1993.
44. Tribouillard, N.; Algeo, T.J.; Lyons, T.; Riboulleau, A. Trace metals as paleoredox and paleoproductivity proxies: An update. *Chem. Geol.* **2006**, *232*, 12–32. [[CrossRef](#)]
45. Cao, H.; Hu, J.; Xi, D.; Peng, P.; Lei, Y. Geochemical characteristics of hydrocarbon source rock and paleoenvironment reconstruction in Houjingou profile of Songliao Basin. *Acta Sedimentol. Sin.* **2015**, *33*, 1043–1052.
46. Zhang, T.; Sun, L.; Zhang, Y.; Cheng, Y.; Li, Y.; Ma, H.; Lu, C.; Yang, C.; Guo, G. Geochemical characteristics of the Jurassic Yan’an and Zhiluo formations in the Northern margin of Ordos basin and their paleoenvironment implications. *Acta Geol. Sin.* **2016**, *90*, 3454–3472.
47. Shi, J.; Zou, Y.; Yu, J.; Liu, J. Paleoenvironment of organic-rich shale from the Lucaogou formation in the Fukang sag, Junggar basin, China. *Nat. Gas Geosci.* **2018**, *29*, 1138–1150.
48. Algeo, T.J.; Maynard, J.B. Trace-element behavior and redox facies in core shales of Upper Pennsylvanian Kansas-type cyclothems. *Chem. Geol.* **2004**, *206*, 289–318. [[CrossRef](#)]
49. Xiang, F.; Song, J.; Luo, L.; Tian, X. Distribution characteristics and climate significance of continental special deposits in the Early Cretaceous. *Earth Sci. Front.* **2009**, *16*, 48–62.
50. Talbot, M.R. A review of the palaeohydrological interpretation of carbon and oxygen isotopic ratios in primary lacustrine carbonates. *Chem. Geol. Isot. Geosci. Sect.* **1990**, *80*, 261–279. [[CrossRef](#)]
51. Chivas, A.R.; De Deckker, P.; Cali, J.A.; Chapman, A.; Kiss, E.; Shelley, J.M.G. Coupled stable-isotope and trace-element measurements of lacustrine carbonates as paleoclimatic indicators. In *Climate Change in Continental Isotopic Records*; Swart, P.K., Lohmann, K.C., McKenzie, J., Savin, S., Eds.; American Geophysical Union: Washington, DC, USA, 1993; pp. 113–121.
52. Rozanski, K.; Araguás-Araguás, L.; Gonfiantini, R. Isotopic patterns in modern global precipitation. In *Climate Change in Continental Isotopic Records*; Swart, P.K., Lohmann, K.C., McKenzie, J., Savin, S., Eds.; American Geophysical Union: Washington, DC, USA, 1993; pp. 1–36.
53. Xi, D.; Wan, X.; Li, G.; Li, G. Cretaceous integrative stratigraphy and timescale of China. *Sci. China Earth Sci.* **2019**, *62*, 256–286. [[CrossRef](#)]
54. Huber, B.T.; Norris, R.D.; MacLeod, K.G. Deep-sea paleotemperature record of extreme warmth during the Cretaceous. *Geology* **2002**, *30*, 123–126. [[CrossRef](#)]
55. Wang, Y.; Huang, C.; Sun, B.; Quan, C.; Wu, J.; Lin, Z. Paleo-CO<sub>2</sub> variation trends and the Cretaceous greenhouse climate. *Earth-Sci. Rev.* **2014**, *129*, 136–147. [[CrossRef](#)]
56. Sellwood, B.W.; Valdes, P.J. Mesozoic climates: General circulation models and the rock record. *Sediment. Geol.* **2006**, *190*, 269–287. [[CrossRef](#)]
57. Hay, W.W. Toward understanding Cretaceous climate—An updated review. *Sci. China Earth Sci.* **2017**, *60*, 5–19. [[CrossRef](#)]
58. Wu, H.; Ren, Y.; Li, J.; Liu, H.; Deng, H.; Zhang, H. Developed characteristics and genetic mechanism of high-quality source rocks in Wuerxun-Beier sags. *Pet. Geol. Oilfield Dev. Daqing* **2014**, *33*, 154–161.

59. Xie, M.; Ma, F.; Chen, G. Petroleum generation kinetics and geological implications for Jurassic hydrocarbon sources rocks, Hongqi depression, Hailar basin, Norgheast China. *Acta Geol. Sin.* **2023**, *97*, 548–561. [[CrossRef](#)]
60. Xie, M.; Chen, G.; Li, J.; Ma, F.; Song, X. Hydrocarbon generation kinetics of source rocks of the first member of Nantun Formation in peripheral sags of Hailar Basin. *Lithol. Reserv.* **2020**, *32*, 24–33.

**Disclaimer/Publisher’s Note:** The statements, opinions and data contained in all publications are solely those of the individual author(s) and contributor(s) and not of MDPI and/or the editor(s). MDPI and/or the editor(s) disclaim responsibility for any injury to people or property resulting from any ideas, methods, instructions or products referred to in the content.